Ultra Low Surface Brightness Imaging with the Dragonfly Telephoto Array

Roberto G. Abraham[1] & Pieter G. van Dokkum[2]

ABSTRACT

We describe the Dragonfly Telephoto Array, a robotic imaging system optimized for the detection of extended ultra low surface brightness structures. The array consists of eight Canon 400 mm $f/2.8$ L IS II USM telephoto lenses coupled to eight science-grade commercial CCD cameras. The lenses are mounted on a common framework and are co-aligned to image simultaneously the same position on the sky. The system provides an imaging capability equivalent to a 0.4 m aperture $f/1.0$ refractor with a $2.6^\circ \times 1.9^\circ$ field of view. The system is driven by custom software for instrument control and robotic operation. Data is collected with non-common optical paths through each lens, and with careful tracking of sky variations in order to minimize systematic errors that limit the accuracy of background estimation and flat-fielding. The system has no obstructions in the light path, optimized baffling, and internal optical surfaces coated with a new generation of anti-reflection coatings based on sub-wavelength nanostructures. As a result, the array's point spread function has a factor of ~ 10 less scattered light at large radii than well-baffled reflecting telescopes. As a result, the Dragonfly Telephoto Array is capable of imaging extended structures to surface brightness levels below $\mu_B = 30\,\mathrm{mag\,arcsec^{-2}}$ in $\sim$10h integrations (without binning or foreground star removal). This is considerably deeper than the surface brightness limit of any existing wide-field telescope. At present no systematic errors limiting the usefulness of much longer integration times has been identified. With longer integrations (50-100h), foreground star removal and modest binning the Dragonfly Telephoto Array is capable of probing structures with surface brightnesses below $\mu_B = 32$ $\mathrm{mag\,arcsec^{-2}}$. The detection of structures at these surface brightness levels may hold the key to solving the 'missing substructure' and 'missing satellite' problems of conventional hierarchical galaxy formation models. The Dragonfly Telephoto Array is therefore executing a fully-automated multi-year imaging survey of a complete sample of nearby galaxies in order to undertake the first census of ultra-faint substructures in the nearby Universe.

Subject headings: cosmology: observations — galaxies: evolution — galaxies: halos — galaxies: photometry — instrumentation: miscellaneous — techniques: image processing — telescopes

1. Introduction

In this article we describe a telescopic imaging system that has been developed in order to explore the Universe at surface brightness levels below $\mu_B = 30$ $\mathrm{mag\,arcsec^{-2}}$. Our primary goal is to test predictions that at very low surface brightness levels galaxies display a wealth of structures that are not seen at higher surface brightness levels.

In a dark energy-dominated cold dark matter (ΛCDM) Universe with largely scale-invariant dark matter halos, $L \gtrsim L_*$ galaxies are thought to be very efficient in accreting smaller neighbors. This infall and accretion process leaves tell-tale features: streams left behind in the wake of the accreted satellites, and tidal distortions and tails. These features should have lifetimes of up to half the Hubble time, so every large galaxy in the Universe is expected to live in an extended, irregular tidal debris field (e.g., Dubinski et al. 1996; Moore et al. 1999; Naab et al. 2007; Kazantzidis et al. 2008; Cooper et al. 2010, 2013).

Although tidal features in galaxies have been identified and studied for many decades (e.g., Toomre & Toomre 1972), a minority of elliptical galaxies and the vast majority of spiral galaxies appear stubbornly unperturbed, even in deep images (e.g., Barton & Thompson 1997; Fry et al. 1999; van Dokkum 2005; Atkinson et al. 2013, and many other studies of individual objects or small samples). A possible explanation for this 'missing substructure problem' is that we have not yet probed the required surface brightness limits to detect the predicted structures. Detailed simulations of tidal debris around Milky Way-like galaxies (Johnston et al. 2008; Cooper et al. 2010) and elliptical galaxies (Naab et al. 2007) indicate that the majority of accreted stars live at surface brightness levels $\gtrsim 29\,\mathrm{mag\,arcsec^{-2}}$. However, deep imaging surveys with standard reflecting telescopes typically reach surface brightness levels of 'only' $\sim 28\,\mathrm{mag\,arcsec^{-2}}$ (e.g. van Dokkum 2005; Tal et al. 2009; Martínez-Delgado et al. 2010; Atkinson et al. 2013). Therefore it is natural to suspect that the 'missing substructure problem' finds its origin in the limitations of our telescopes for undertaking low surface brightness imaging. A related issue, the 'missing satellites problem' (in which the number of dwarf galaxies in the local group is orders of magnitude lower than expected from numerical simulations) may have a similar solution, if the missing satellites have very low surface brightnesses.

Imaging to surface brightnesses fainter than $\sim 28\,\mathrm{mag\,arcsec^{-2}}$ has proven very difficult. It is rather striking to note that the present limit is not significantly deeper than that reached by researchers undertaking very long photographic integrations four decades ago (e.g. Kormendy & Bahcall 1974). Over the same period of time, revolutionary advances in detector technology have pushed back the ground-based limit for galaxy detection by over five magnitudes, transforming the study of intrinsically faint but relatively small targets.

The reason for the slow progress in lowering the limit for the detection of low surface brightness structures is due to the fact that the limit is not defined by photon statistics, but rather by systematic errors. The most obvious of these is the error introduced by imperfect flat fielding. Flat fielding errors need to be smaller than 0.1 % to reach $\sim 30\,\mathrm{mag\,arcsec^{-2}}$. This is challenging, but it is achievable if careful procedures are adopted. More difficult problems that must be overcome include ghosting and diffraction, which together result in a complex and spatially variable low-surface brightness point spread function (PSF) at large angles. This faint component of the PSF is ignorable in most applications, but it plays a central role at low surface brightness levels. For example, Slater et al. (2009) show that even with a telescope that is highly optimized for low surface brightness imaging, diffraction from the secondary mirror assembly, coupled with scattering and internal reflections in the optical train and microroughness in aluminized optical surfaces, produces a complex emission structure that fills the entire imaging frame below $\sim 29\,\mathrm{mag\,arcsec^{-2}}$. Interestingly, it appears that several of the the basic design trades that make large telescopes possible (in particular, obstructed pupils and reflective surfaces) define the fundamental systematic errors that make pushing to very low surface brightnesses so difficult.

At present the surface brightness levels needed to test the missing substructure problem have only been approached on a few occasions. Mihos and collaborators have imaged the center of the Virgo cluster down to $\sim 29\,\mathrm{mag\,arcsec^{-2}}$ using extremely long exposures with the low surface-brightness-optimized, 0.9 m Burrell Schmidt telescope on Kitt Peak. These authors discovered a wide array of tidal features and complex structures in the intra-cluster light (Mihos et al. 2005). The same group has probed M101 down to comparable limits using the same telescope and ray-traced removal of contaminating stellar halos (Mihos et al. 2013). Even fainter limits have been reached in the Local Group, through counts of individual stars. Both the Milky Way and M31 are embedded in a complex network of streams and tails, which extend out to several hundred kpc (Ibata et al. 2001; Belokurov et al. 2007; McConnachie et al. 2009). The imaging system described in this paper should be capable of detecting and characterizing such structures — if they exist — around any galaxy in the nearby Universe.

2. Concept

The optics of a low surface brightness-optimized telescope should have the following characteristics: no reflective surfaces, because dust and microroughness on metallic coatings backscatter light into the optical path[3]; an unobstructed pupil, because any central obstruction causes diffraction which moves energy into the wings of the PSF; nearly perfect anti-reflection coatings, so that ghosts and flaring do not strongly pollute the focal plane; and a small (fast) focal ratio, as the imaging speed for extended structures much larger than the resolution limit depends on the focal ratio, not the aperture.[4]

Combined, these characteristics describe a fast *refracting* telescope. Large refractors are not commonly used in contemporary astronomical research, and the largest remains the 1.02m $f/19$ Yerkes achromat. The textbook limitation on large refractor telescopes is chromatic aberration, but this aberration can be well controlled using an appropriate combination of modern glasses (and glass-like crystals), and other issues provide the main challenges in building large refractors. These include the difficulty of supporting large and thin optics at their edges, and the requirement that the transparent materials used be internally very homogeneous. Overcoming these limitations is expensive at large apertures. As a result, at present the main place for large and fast refractive optics in astronomical research is within the re-imaging cameras of large reflecting telescopes. Several of these cameras have multiple lenses bigger than the objective lens of the Yerkes telescope.

Nevertheless, very fast refracting telescopes do exist in large numbers, and they are called telephoto lenses. The fastest commercial telephoto lenses have focal ratios of $f/2.8$ and focal lengths of up to 500 mm. These fast, long lenses have been developed for professional sports and wildlife photographers, who often need to freeze distant action in low or mixed lighting conditions. The best lenses have very low optical distortions, and because they must sometimes be used when pointed near the sun, many are extremely well baffled. Invariably they feature a fully enclosed structure with a large hood which also assists in controlling scattered light.

A potential downside to these lenses is that they have many optical elements, which makes it difficult to control internal reflections. However, the latest generation of Canon lenses features the first commercialized availability of nano-fabricated coatings with sub-wavelength structure on optical glasses. The surface of these coatings resembles a grid of cones whose separation is less than a wavelength of light. An incoming wavefront averages over an increasing impact factor of coating material as it propagates through to the glass, yielding an effective continuous variation in the index of refraction and over a factor of ten improvement in the suppression of scattered light and internal reflections, even on steeply curved optical surfaces. Remarkably, as a result of these coatings, in terms of overall optical quality over a very wide field, at present no optically fast astronomical telescope is equal to the latest generation of commercial telephoto lenses that use this technology.

Commercially available telephoto lenses are all of relatively small aperture. As we have already noted, imaging speed to a given surface brightness limit depends on focal ratio and not on the aperture. Aperture is certainly very significant, however, since it defines the focal length at a given focal ratio, and the focal length must be adequate to allow the desired angular resolution to be achieved. The needed angular resolution needs to be traded off against the desired field of view. A field of view of several degrees is desirable, because nearby galaxies are enormous at low surface brightness levels. For example, extrapolation of the profile of typical Virgo cluster elliptical suggests angular diameters of over a degree at surface brightness levels around 30 mag arcsec^{-2}. Ideally, such large areal coverage would be achieved without the need for mosaiced detectors, which can add significant challenges to low surface brightness imaging.

The Dragonfly Telephoto Array[5] concept (shown

[3] This is one reason why many coronagraphs and some high-contrast imaging systems eschew reflective optics; see Nelson et al. (2008).

[4] A standard 50 mm f/1.8 consumer camera lens has the same 'light gathering power' as the Keck telescope when expressed as the number of photons per unit detector surface. The difference is that Keck images an area of the sky that is 40000× smaller. We go into this in greater detail in Section 5.

[5] We chose to name the concept the Dragonfly Telephoto Ar-

Fig. 1.— The Dragonfly Telephoto Array installed at the New Mexico Skies telescope hosting facility. The array consists of eight Canon 400/2.8 L IS II USM telephoto lenses attached to eight SBIG STF-8300M CCD cameras, all carried by a Paramount ME-II german equatorial mount. The system is controlled by the three computers shown in the foreground.

in Figure 1) is an attempt to balance these factors. It is a wide-field visible-wavelength imaging system with significant aperture created by synthesizing a "compound eye" with multiple Canon 400 mm $f/2.8$ IS II telephoto lenses. This particular lens model is the the longest commercially-available $f/2.8$ lens featuring the nano-fabricated coatings. Each lens has an aperture of 143mm.[6] By creating an array, the effective aperture is increased while the focal length remains fixed at 400 mm, thus further increasing the imaging speed of the system. Each lens is outfitted with its own monolithic CCD camera, and by combining the light from all the cameras the effective aperture for N lenses is $\sqrt{N} \times 143$ mm and the effective focal ratio is $2.8/\sqrt{N}$. While the diffraction-limited angular resolution of the array remains that of a single 143mm aperture lens, this is small enough ($\sim 0.65''$ at 450nm) to be seeing-limited most of the time at most dark sites in the continental USA.

3. The Dragonfly Telephoto Array

We have built and are operating the Dragonfly Telephoto Array with $N = 8$ lenses as a collaboration between the University of Toronto and Yale University. In this section we will describe the array in its present 8-lens configuration. The present system can accommodate up to 15 lenses with only minor modifications, and we expect to increase N gradually with time. Even larger systems can be constructed by upgrading the existing mount.

3.1. Lens and Camera Components

Canon 400 mm f/2.8 IS II lenses form the heart of the Dragonfly Telephoto Array. The first generation of these lenses came out in 1996. The second generation features the nano-fabricated coatings discussed in § 2, and became available in August

ray for the following reasons. (1) We took inspiration from the the compound eyes of insects when developing the central ideas behind the array; (2) The operational concepts that form the basis of the critical sub-wavelength nanostructure coatings were discovered by researchers investigating the unusually high transmittance of insect wings; (c) One of the authors really likes taking pictures of Dragonflies.

[6]The only telephoto lens we are aware of with a larger aperture is the Sigma $f/2.8$ 200 mm – 500 mm zoom lens, nicknamed "Bigma".

2011. The optical design of the lenses is proprietary, but published sources indicate that the latest model has 17 optical elements arranged in 13 groups. Each lens has an internal autofocusing motor (which our system takes advantage of) and an image stabilization ("IS") unit to compensate for small motions in hand-held operation (which our system presently does not use – image stabilization is permanently switched off in our application). Each lens can be stopped down with a diaphragm, enabling operation from $f/2.8$ to $f/32$. We operate the lenses at the widest aperture, $f/2.8$, only. At $f/2.8$ the aperture of each lens is 143 mm. The relative angular positions of lenses are slightly offset from each other in order to facilitate the data reduction process (since residual ghosting and flaring is displaced differently on each lens).

Each of the eight lenses in the array is connected to a Santa Barbara Imaging Group (SBIG) STF-8300M CCD camera. These cameras have Kodak KAF-8300 CCD detectors, which have a 3326×2504 pixel format. The quantum efficiency of the cameras is shown in Fig. 2, and peaks at 58% at 550nm. The mean efficiency of the detector + filter combination is 34% in g-band and 43% in r-band. The pixel size is $5.4\,\mu$m, which corresponds to $2\farcs8$/pixel. With 400mm lenses the field of view of the system is $2.6° \times 1.9°$. The detectors are cosmetically excellent and have no bad columns. Illumination of the field is quite uniform, dropping by only $\sim 20\%$ from centre to corner. The read noise of each detector is around 10 electrons (varying by $< 10\%$ from detector to detector) and the gain is preset by the manufacturer to 0.37 electron/ADU. The cameras are temperature regulated using a thermo-electric cooler. Operating at $-10°$ C the measured dark current is around 0.04 electron/s (varying negligibly from detector to detector). Dark noise is removed using dark frames obtained roughly every 90 minutes, although in practice the dark frames are very stable from night-to-night.

Each lens is equipped with a filter via an internal drop-in filter holder. We have obtained custom SDSS g and r filters from Astrodon Imaging, Inc. The filter curves are overplotted in Fig. 2. We simulated the signal-to-noise (S/N) ratio in filtered and unfiltered images using the quantum efficiency curve and template spectra for the sky emission,

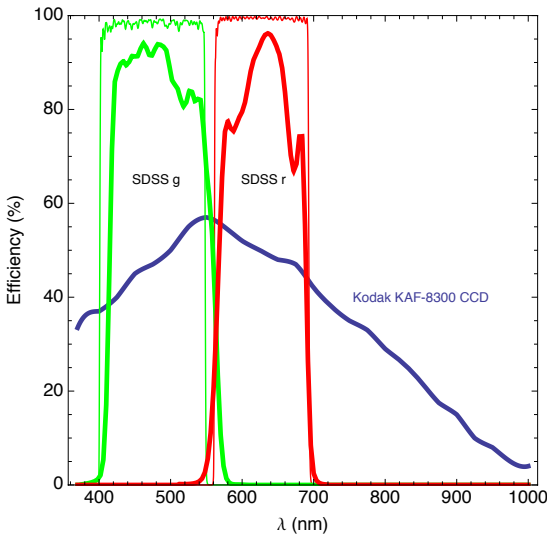

Fig. 2.— Sensitivity of the Kodak KAF-8300 CCDs with the transmission curves of the g and r filters overplotted. These filters are inserted into the drop-in filter holder slots of the Canon lenses. Green and red curves drawn with thin lines are manufacturer-supplied laboratory measurements of throughput for our Astrodon g and r filters. These were determined using a collimated beam. Green and red curves drawn with thick lines are laboratory measurements for the CFHT MegaCam SDSS filters made with an $f/8$ converging beam.

sky absorption, and an early-type galaxy. We find that the S/N ratio is approximately equal in g and r in equal exposure times. Compared to an unfiltered image the S/N is approximately $\sqrt{2}$ times lower in each filter; that is, not much could be gained by using broader filters than g and r. In typical use, half the lenses image in g and half in r. This minimizes the impact of systematic errors when determining colours, since the colours are obtained using data taken contemporaneously in both filters. Typical integration times are 600s in both g and r, which assures that all exposures are sky-noise limited.

Because of the speed of the lenses, maintaining precise focus is a challenge. At $f/2.8$ the linear diameter of the airy disk on the detector is $d = 3.1\mu$m at 450nm. The depth of focus is $2fd$, corresponding to 17μm. The opto-mechanical design of the lenses does not incorporate temperature compensation at this level, and focus changes become noticeable when the ambient temperature varies by as little as 1°C. Therefore, frequent and robust focusing is essential. The Dragonfly lenses are focused using their internal autofocusing motors. These motors are driven by custom adapters, made by Birger Engineering Inc, which connect the SBIG cameras to the lenses. The adapters have no optics and do double duty as spacers necessary to project the focal plane onto the CCD. The internal stepping motors are fast and allow movements of 20,000 digital set point increments (covering the full mechanical motion of the internal focus mechanism) in under 1s. A digital step corresponds to about 3.15μm of focus motion. Focus is determined automatically using scripts which take a set of very short integrations in each camera and run each resulting frame through SExtractor (Bertin & Arnouts 1996). The scripts fit a parabola to the run of full-width at half-maximum (FWHM) vs. digital set point values and leave the focus set at the minimum FWHM position. The initial focus positions for the eight lenses are determined in a 24 point focus run (taking about seven minutes) during twilight at the start of each night. The focus positions are then adjusted with short focus runs every 90 minutes (each taking under 5 minutes). Temperature is monitored throughout the night and in between focus runs the focus is adjusted after each integration in an open loop fashion using a temperature model we have built up using archival focus positions[7].

3.2. Structure and Mounting

In terms of pointing, slewing, and other mount control operations the Dragonfly Telephoto Array is effectively a single telescope. The lenses and cameras are mounted together on a rigid box-like aluminium framework. The main structural elements of the framework are constructed from 25mm thick aluminium struts. A finite element analysis was used to model this framework prior to deployment in order to ensure that the main bending mode of the framework is predominantly orthogonal to the optical axes of the lenses when the structure is pointed at targets at low airmass, so that any residual flexure can be guided out by a single auto guider sharing the framework with the lenses. In practice, at low airmass the main sources of flexure are the stock mounting feet used to mount the lenses onto the framework. Use of these feet alone resulted in significant flexure, ruining around 30% of the integrations. This was fixed by augmenting the stock mounting feet with three-point ring harnesses that grip the lenses firmly near their front elements. After this minor change flexure is negligible in 10 minute integrations taken within 45 degrees of the zenith[8].

The lens framework is mounted on a Paramount ME II german equatorial mount manufactured by Software Bisque, Inc. The total weight of the system (mounting framework + lenses + cameras + cabling) is $\sim$ 80kg, which is easily handled by this equatorial mount, which has a conservatively rated instrument capacity of 110kg. When used with short focal length instruments (such as telephoto lenses) the Paramount ME II is likely to be able to support an instrument load of over 140kg while maintaining excellent tracking accuracy. In addition to its rated capacity, the main feature of this

[7] It is interesting to note that although each lens operates at a focal ratio $f/2.8$ the total system operates at an effective focal ratio of $f/1.0$. A monolithic camera operating at $f/1.0$ would have a depth of focus of only 2μm, and maintenance of of accurate focus would be much more challenging than it is with the Dragonfly Telephoto Array.

[8] At lower air masses flexure is noticeable in 10 min integrations and integration times are generally kept to less than 5 minutes. For our galaxy survey there are always ample targets at low airmass, but in future we will improve the stiffness of the structure to better enable side-projects to be undertaken with the Dragonfly Array.

mount that makes is suitable for robotic operation is its incorporation of an absolute homing sensor on each axis, which means it can recover its absolute position on the sky after a power failure or other untoward incident.

All-sky pointing of the equatorial mount is accurate to better than 20 arcsec after the incorporation of a 300 position pointing model constructed with the `TPOINT` mount modelling software (Wallace 1994). In order to refine pointing even further, our control software does an astrometric plate solve of a short integration after each long slew, resulting in absolute positions accurate to a few arcseconds. After an empirically-derived periodic error correction the root-mean-square tracking error of the mount is below 1.5 arcsec. Because our pixels are 2.85 arcsec in size, stars are generally quite round even in unguided 600s integrations. However in order to obtain the best possible image quality an autoguider is generally used. The latest version of our control software automatically finds suitable guide stars and our reduction pipeline rejects frames in which the axial ratio of stars deviates from perfect roundness by more than 15% over most of the frame.

3.3. Functional Operation and Control Software

A functional overview of the Dragonfly Telephoto Array is presented in Figure 3. The system is controlled by three separate computers which communicate with each other over TCP ports using software we have written and released into the public domain[9]. In practice, the user is shielded from most of the details shown in the Figure.

The user of the Dragonfly Telephoto Array array interacts only with a single computer known as the *master control computer*. This is a UNIX-based system running the Mac OS X operating system. The only tasks needed to be undertaken by the user are to log in to this computer in the afternoon, edit and execute a small shell script (indicating the desired targets for the night's observing) and then download the data the following morning. A sample shell script is shown in Appendix A, which documents the required procedure. All other activity undertaken by the Dragonfly Telephoto Array is fully automated. Behind the scenes, the master control computer interfaces with a weather monitor to determine whether it is worthwhile acquiring data, operates the focuser controllers to focus the array, sends pointing and tracking commands to the equatorial mount and autoguider (via `TheSkyX`, a proprietary program written by the mount manufacturer) and sends commands to separate computers over the network to control the operation of the cameras. Each computer controls up to four cameras[10]. During the night, images from the observatory's all-sky camera, the results from automated focus runs, and graphical summaries of image quality and other information are emailed at regular intervals to a special account. These constitute a comprehensive night log.

Each camera control computer runs a high-level network-aware server which listens for commands from the master control computer and returns diagnostic information to it. The four cameras on each camera control computer are read out serially (taking < 30s to readout all four cameras), but each camera control computer operates in parallel with the others. Therefore an arbitrary number of additional lenses and cameras can be added to the array without adding any extra overhead. The only constraint on adding additional lenses and cameras to the system is that an additional camera control computer must be added for every four cameras added.

3.4. Site

The Dragonfly Telephoto Array is located at the New Mexico Skies telescope hosting facility[11] near Cloudcroft, NM. The site is in the Sacramento Mountains at an altitude of 2200 m. It is located about 30km from Apache Point Observatory and is significantly darker, as it is further away from the town of Alamogordo. Although no long-term averaged measurements of the sky brightness are available, the site appears to be one of the darkest in the Continental USA.[12] The seeing at the New Mexico Skies site is rarely subarcsecond (and typical long-exposure seeing is 1.5

[9] https://github.com/robertoabraham/ProjectDragonfly

[10] The limitation of at most four USB cameras per computer is set by the SBIG Universal Library, which provides the camera control API against which our software is written.

[11] http://www.nmskies.com/

[12] http://www.jshine.net/astronomy/dark_sky/

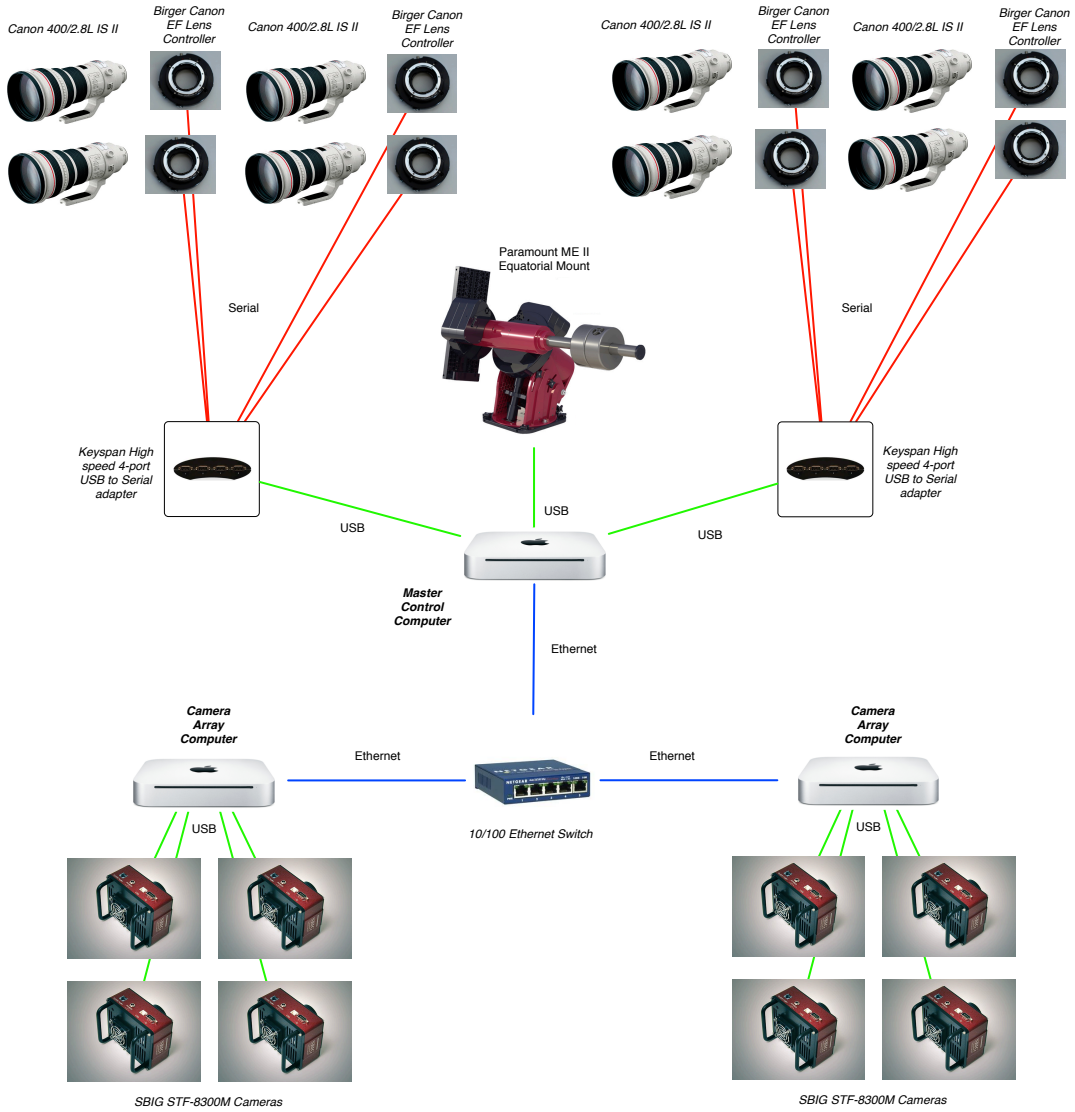

Fig. 3.— A functional overview of the Dragonfly Network Array. Serial connections are shown in red, USB connections are shown in green, and ethernet connections are shown in blue. The lenses are mechanically connected to the CCD cameras via focus controllers which in turn are connected to the master control computer via serial lines. Each group of four cameras is connected to a separate camera control computer via USB connections. Interprocess communication between all computers occurs via TCP/IP sockets. See text for details.

– 2 arcsec). Our images are under sampled and the site seeing is not a significant limiting factor in our observations.

New Mexico Skies is host to a large number of small robotic telescopes that are mostly owned and operated by advanced amateur astronomers, although other institutional clients include Caltech, NASA, and NOAO. The Dragonfly Telephoto Array is presently mounted on a steel pier in a large roll-off roof shed which is shared by about ten other telescopes. The roof is closed during the day and in adverse weather conditions. The facility is responsible for opening and closing the roof and for basic maintenance of the Dragonfly Telephoto Array, including regular nonabrasive cleaning of optical surfaces using a CO_2 snow cleaning system.

4. Image Quality

4.1. Resolution and field uniformity

An analysis of the image quality delivered by a typical lens-camera unit is presented in Figure 4. This analysis is based on a raw data frame, and shows most of the salient features (including common imperfections) in the data. The figure displays four panels corresponding to the background sky level, full-width at half maximum of the point spread function (PSF), ellipticity of the PSF, and position angle of the PSF. Distributions of these quantities were obtained by fitting 3rd order polynomials to results obtained by SExtractor (Bertin & Arnouts 1996) for $\sim$ 500 unsaturated stars in the image. The FWHM values were estimated using the `FWHM_IMAGE` parameter returned by SExtractor after filtering out galaxies and saturated stars using the `CLASS_STAR` and `FLAGS` parameters. Stellar images perfectly centred on a pixel have a FWHM $\sim$ 1.5 pixel, as expected for undersampled images of $\sim$ 2 arcsec FWHM stars imaged by an optical system whose intrinsic angular resolution is higher than the 2.85 arcsec sampling resolution of the detector.

The illumination pattern is well-centered on the chip, indicating good overall collimation of the optical components in the lens. The illumination drops by approximately 20% from centre to edge. There is a small gradient in the delivered FWHM values in the top-right panel. Variations in FWHM at the 10% level are commonly seen, and they usually find their origin in the mechanical precision of the interface between the lenses and the cameras. At $f/2.8$ even slight mis-collimation leads to visible image degradation, and this is exacerbated by the fact (already noted) that the depth of focus is rather shallow in fast optical systems. Precise perpendicularity between the CCDs and the optical axes of the lenses is required for the best image quality. In the example shown a slight tilt in the focal plane is seen. This only impacts the image quality at a low level and it has negligible impact on our science goals[13]. Another minor source of image degradation is imperfect tracking or guiding, which manifests itself by slightly out of round stars with position angles oriented in the Right Ascension direction. Tracking is sufficiently good that autoguiding is not always required, but for the sake of caution we generally do autoguide, although with quite long integration times (5–10s) which ensure a guide star is always available. Stellar images on our raw data frames are typically quite round, with deviations at the 10–15% level, which is adequate for our science. In future we will probably upgrade the autoguider to improve image quality further.

Telephoto lenses are generally optimized for minimal chromatic aberration, excellent field flatness, high illumination over a large area, relatively low distortion, and other factors. However, they are not usually designed to be diffraction limited at full aperture. Indeed, as noted earlier, our configuration's 2.85 arcsec pixels greatly undersample a diffraction limited instrument with the 143mm aperture of a single lens. Nevertheless, the particular model of Canon lens chosen for use in the Dragonfly Telephoto Array is reputed to be amongst the sharpest currently available[14], so curiosity drove us to explore the ultimate resolution limit of the lenses, even though our project does not exploit this. We investigated the on-axis image quality of the lenses using a curvature wavefront estimator outlined in Roddier & Roddier (1993).

[13] One of the authors is congenitally unable to leave well enough alone, so at some point in the future we expect to shim the focus controller's mechanical spacers until the tilt in the focal plane contributes < 0.1 pixel to the total FWHM budget.

[14] Modulation transfer functions for most Canon lenses are available in Chapter 10 of the *Canon EF Lens Work Book* which can be downloaded from `http://software.canon-europe.com`.

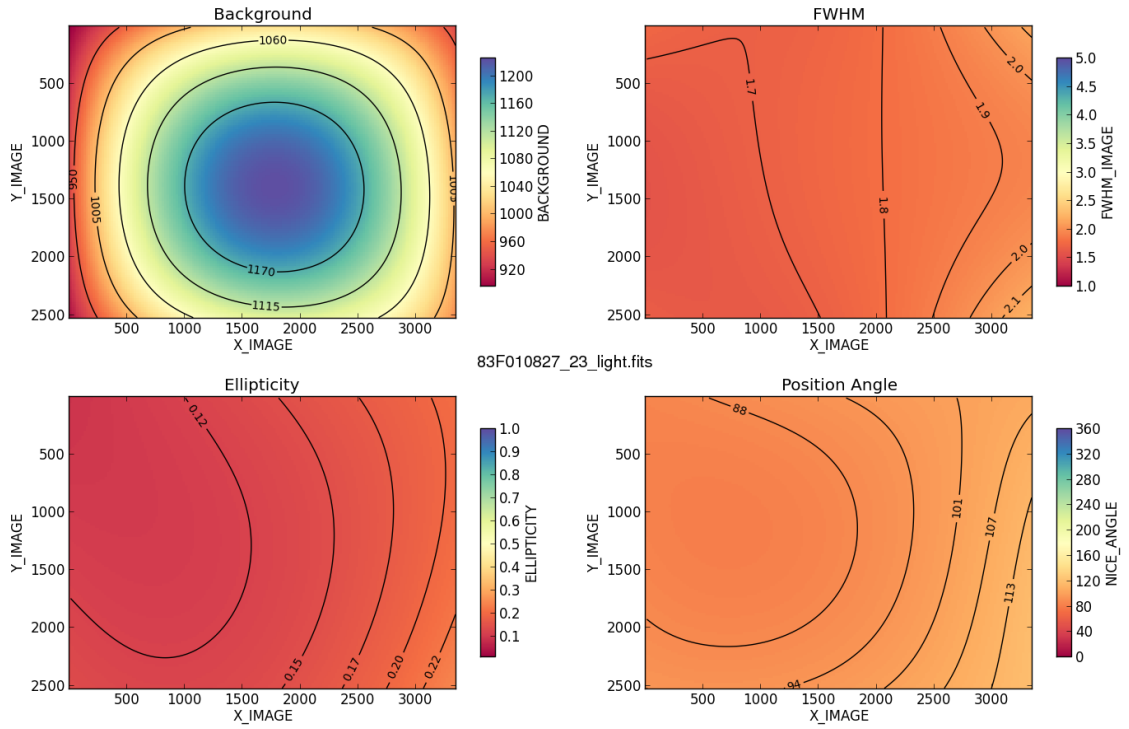

Fig. 4.— Image quality maps obtained from a typical raw data frame, illustrating the uniformity over the field from a single lens-camera unit. The distribution of quantities shown were obtained by fitting a 3rd order polynomial to results obtained by SExtractor (Bertin & Arnouts 1996) for ~ 500 unsaturated stars. The target was a low galactic latitude field imaged for 600s. (Top left:) Background in counts. The illumination drops by approximately 20% from centre to edge. (Top right:) Full-width at half maximum (FHWM) in pixels. At 2.85 arcsec/pixel the images are under sampled. FWHM values were determined using SExtractor's `FWHM_IMAGE` parameter. Stars perfectly centered on a pixel have FWHM ~ 1.5 pixel (the lowest possible using SExtractor's algorithm for estimating FWHM in very undersampled images). The average FWHM is below 2 pixels over the entire frame. Note the mild gradient in image quality. This is due to a combination of intrinsic aberrations in the optical design of the lens, a modest amount of field curvature and slight tilt in this particular camera-lens unit's focal plane. The maximum FWHM degradation due to the tilt is 0.4 pixel across the frame and focal plane is tilted at an angle of about 90 degrees. (Bottom left): ellipticity from stellar sources. The ellipticity is below 15% over most of the field. (Bottom right): Position angle in degrees relative to the X-axis. At the orientation of the camera the prevailing elongation is along the RA axis, indicative of slight tracking imperfections that were not fully guided out.

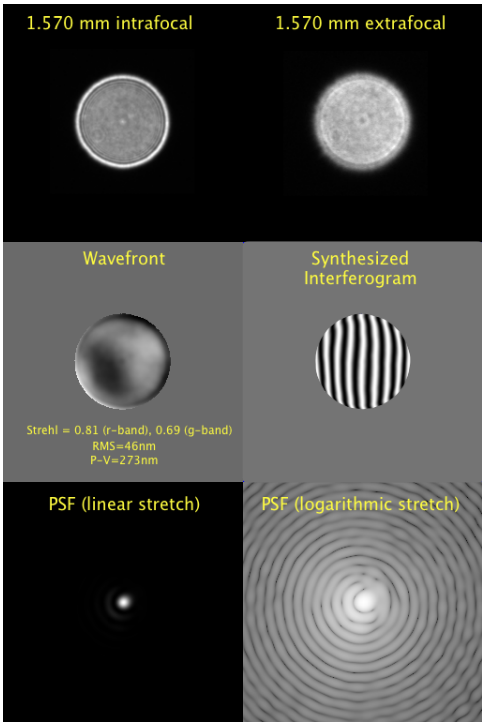

Fig. 5.— Results from a wavefront curvature analysis of one of the better Canon lenses in the Dragonfly Telephoto Array. Quantities were obtained using the methodology outlined in Roddier & Roddier (1993). All results shown were obtained from two 0.5s integrations of Vega. [Top row:] intrafocal (left) and extrafocal (right) short-exposure images obtained in r-band. The defocus was 1.574mm (500 digital set points). Note the Fresnel rings are much softer in the extra-focal image. This is indicative of significant aberrations in the wavefront. [Middle row:] The computed wavefront (left) and the corresponding synthetic interferogram (right). The RMS error in the wavefront is 46nm. This gives a Strehl ratio of 0.81. [Bottom row:] Point-spread function computed from the wavefront in the middle row. The PSF is shown with linear stretch (left) and logarithmic stretch (right). Note that the first airy ring is slightly non-uniform but this non-uniformity disappears at larger angles. See text for details.

In this procedure, the wavefront W can be reconstructed from an intra-focal image $I_{\rm in}$ of a bright star and an extra-focal image $I_{\rm out}$ of the same star by solving a partial differential equation of the inhomogeneous Poisson form:

$$\nabla^2 W \approx k\,\frac{I_{\rm in}-I_{\rm out}}{I_{\rm in}+I_{\rm out}}. \qquad (1)$$

subject to the Neumann boundary condition:

$$\partial W/\partial \vec{n} = 0 \qquad (2)$$

where k is a constant that depends on the degree of defocus and on the focal length of the lens and $\vec{n}$ is a vector normal to the circular boundary of the projection of the pupil on the image plane.

Equation (1) is straightforward to solve using Fourier techniques, and results are presented for one of the better lenses in the array in Figure 5. The RMS error in the wavefront is 46nm, corresponding to a Strehl ratio 0.81 in r-band. The lenses have remarkably good control of chromatic aberration, and the wavefront shape is similar in g-band, corresponding to a formal Strehl ratio of 0.69. Since we estimated the wavefront from two defocused images (one intrafocal, and one extrafocal), both of which were affected by seeing, the delivered Strehl from the optics alone is probably above 0.8 even in g-band. Therefore we suspect this lens is diffraction limited at both wavelengths of interest for our project. However, it is worth noting that the lenses do show quite significant sample-to-sample variation, with a mean Strehl ratio around 0.4 and with the poorest lenses having Strehl ratios as low as 0.2. Interestingly, because of our large pixels, in practice the poorest of our lenses appears to deliver identical performance to the best lenses when investigated using metrics such as those shown in Figure 4. The lower Strehl lenses are only identifiable by mapping their wavefronts, reinforcing our view that the main limiting factor on resolution on our data is detector sampling and not optical quality (or seeing)[15]. For our purposes the most important characteristics of the

[15]Note that much higher Strehl ratios (> 0.95) are attainable in purpose-built astrographs intended to provide high-resolution images of astronomical targets. We considered implementing an array of commercial astrographs, but after looking carefully at the trade-offs involved it was concluded that an array of telephoto lenses was the better choice in our case.

lenses are defined by their scattering and ghosting properties, the investigation of which we turn to next.

4.2. Scattering and ghosting

To examine the scattering and ghosting properties of the Dragonfly Telephoto Array's lenses we imaged Vega and used this to determine the radially-averaged point spread function of one of our lenses out to angular radii around one degree. We wanted to explore contrast ratios of around 10^8:1, which is far more than can be accommodated with a single integration. Therefore the star was imaged at a range of integration times and a series of sub-profiles was constructed. These sub-profiles were stitched together to create the complete profile shown in Figure 6. This figure also shows the published point-spread function from the 0.9 m Burrell Schmidt telescope on Kitt Peak (Slater et al. 2009). The minimum radius plotted is 0.1 arcmin, and $\gtrsim 90\%$ of the total stellar flux is interior to this, so only a small fraction of a star's total light is contained within the wide-angle halo (mainly due to scattering and internal reflections) shown in the figure. The left hand panel of Figure 6 shows flux as a function of linear radius, after normalizing both the Dragonfly and Burrell profiles so they contain identical total fluxes. The right hand panel shows the r-band AB mag/arcsec^2 surface brightness profile of Vega as a function of logarithmic radius. The former is based on direct measurement, but the latter is an estimate based on the profile of Arcturus presented in Slater et al. (2009), who imaged this star in the Washington M-band. In transforming to the Vega profile we accounted for the relative brightnesses of the two stars and the $M-r$ colour of Arcturus.

The Canon lenses in the Dragonfly Telephoto Array show a factor of $5-10$ less scattered light at radii > 5 arcmin than the Burrell Schmidt. The point spread function from the lenses declines more steeply than that of the Burrell Schmidt, and shows fewer bumps from diffraction effects and ghosts. The Burrell Schmidt is a superb instrument that is highly optimized for low surface brightness imaging and it has produced a beautiful and well-known ultra-deep image of the Virgo cluster (Mihos et al. 2005). Therefore we consider the performance of the commercial lens exhibited in Figure 6 to be quite impressive.

What new capabilities for low-surface brightness imaging are opened up by optics that deliver the performance shown in Figure 6? Slater et al. (2009) showed that even at the high galactic latitude of the Virgo cluster ($b \sim 75°$), using the optimized Burrell Schmidt, over 50% of pixels are contaminated by scattered light from faint stars at $\mu = 29$ mag arcsec^{-2}. Figure 6 suggests that equivalent performance can be obtained around two magnitudes fainter using the Dragonfly Telephoto Array. The ramifications of this are displayed in Figure 7. The top panel of this figure shows a small area of an individual 300 s exposure of a crowded galactic field obtained using a single telephoto lens. The bottom panel shows the corresponding area imaged using a combination of many exposures from separate lenses to provide the equivalent of 1183× longer exposure time. The images are stretched to a similar dynamic range. This figure makes two important points. Firstly, in spite of the integration time being over 1000x longer in the bottom panel, the stellar halos are not much bigger. We have not yet encountered systematic errors limiting the usefulness of very long integration times (up to ~ 100 hours) with the Dragonfly Telephoto Array. The second important point is that at very low surface brightness levels even apparently empty patches of sky can be riddled with cirrus. The need for foreground structure avoidance (or removal) will play an important role in defining the strategy for surveys intended to explore faint galactic structures. We will have much more to say about this topic in future papers.

We conclude this section by noting that, in spite of their excellent performance in terms of ghosting and scattered light control, the lenses in our array still have room for some improvement. Figure 8 shows a 1° x 1° subset of an image of Venus imaged near maximum brightness (apparent mag ~ -4) obtained with one of the telephoto lenses. Ghosts and wide-angle diffraction effects in this image are seen at a much lower level than in images obtained with reflecting telescopes (for example, compare this figure with the images of Arcturus shown in Slater et al. 2009), but they are not completely absent. We are uncertain of the origin of the low-level spikes seen in Figure 8. We tentatively attribute them to diffraction from the blades of the

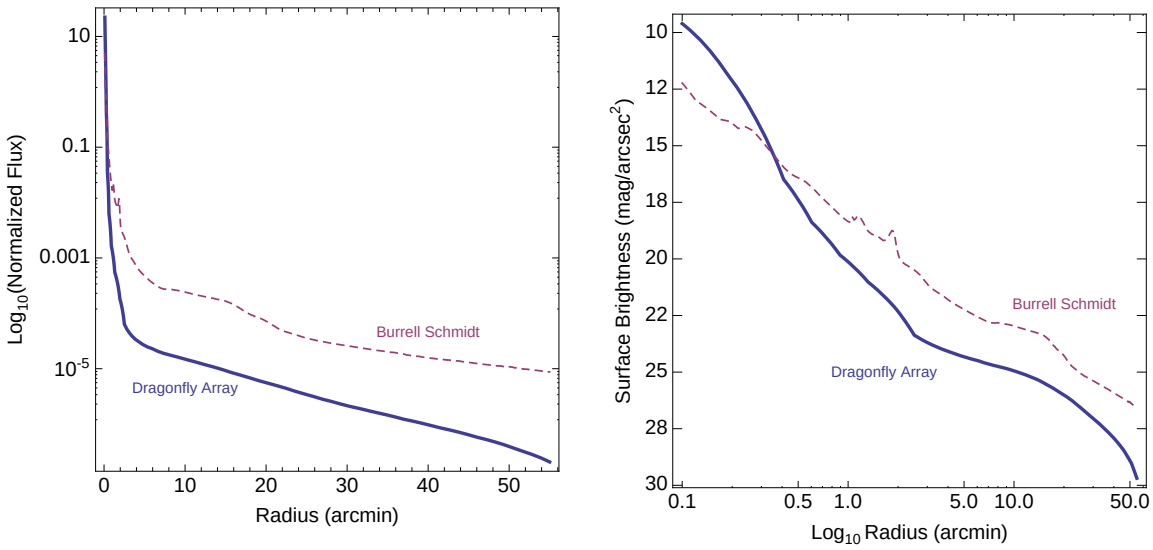

Fig. 6.— Comparison of the wide-angle halo point-spread function of the Canon telephoto lenses used in the Dragonfly Telephoto Array with the corresponding point-spread function of the 0.9 m Burrell Schmidt telescope on Kitt Peak (Slater et al. 2009). The Burrell Schmidt is optimized for low surface brightness imaging and has produced a well-known ultra-deep image of the Virgo cluster (Mihos et al. 2005). The minimum radius plotted is 0.1 arcmin, and in both cases $\gtrsim 90\%$ of the total stellar flux is interior to this, so only a small fraction of a star's total light is contained within the wide-angle halo (mainly due to scattering and internal reflections) shown in these plots. [Left Panel:] Flux as a function of linear radius, after normalizing both profiles to contain identical total fluxes. Note that in large part thanks to nano-fabricated anti-reflection coatings on some of its elements, the Canon lenses have a factor of $5-10$ less halo light at radii > 5 arcmin. [Right Panel:] The r-band AB mag/arcsec^2 surface brightness profile of Vega as a function of logarithmic radius for the Dragonfly Array and for the Burrell Schmidt telescope. See text for details.

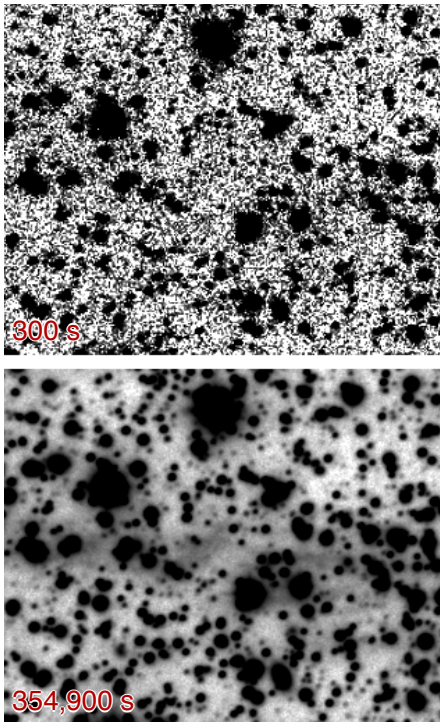

Fig. 7.— Illustration of the excellent control of scattered light in the Dragonfly Telephoto Array PSF. The image is a $13.1' \times 10.5'$ area of crowded sky near the Galactic plane. The top panel shows an individual 300 s exposure obtained with a single telephoto lens. The bottom panel shows a combination of many exposures in order to provide an equivalent of a 1183× longer exposure time. Nevertheless, the stellar halos do not appear much bigger in the bottom image. Note the faint low surface brightness cirrus that is apparent in the combined image. The data in this figure was obtained in a filterless 'white light' configuration and we cannot calibrate the surface brightness of the structure shown, but based upon carefully calibrated data through g-band and r-band observations of M101 (van Dokkum et al. 2013, submitted) it is clear that some of the structures shown are at surface brightnesses below 30 mag arcsec^{-2}.

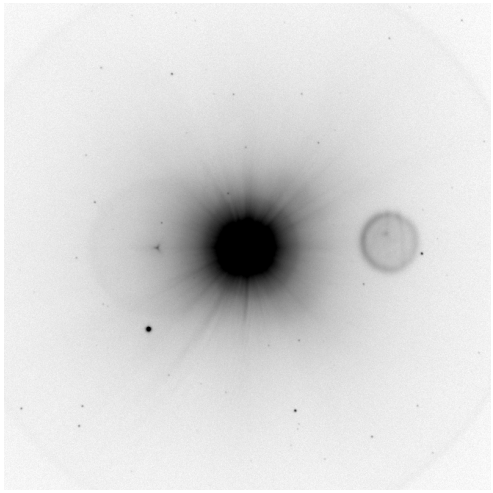

Fig. 8.— A white-light image of the planet Venus, obtained with the one of the Canon 400/2.8 EF IS II telephoto lenses of the Dragonfly Telephoto Array on Nov. 4, 2012. The image spans $50' \times 50'$ is displayed with a logarithmic stretch. The PSF is well behaved out to large radius and shows no strong diffraction spikes and relatively few large ghosts or other asymmetric features. On the date the image was taken Venus was at magnitude −4, and is highly saturated on the frame. However the bright star to the bottom-left of Venus is unsaturated. This is the ∼ 7th magnitude F5 star SAO 138876 ($m_B = 7.42$ mag, $m_V = 6.95$ mag), which can be used as a calibrator. Using this star as a reference, the highest surface brightness ghost has an integrated flux ∼ 9 mag fainter than that of Venus, and contains only ∼ 0.025% of its light.

internal iris in the lens which enters into the edge of the pupil when a target is not perfectly on axis, but it is also possible that at this level there are some contributions to diffraction from striae in the glasses or lattice imperfections in the crystalline optical elements used by the lenses. We attribute the circular ghosts to the fact that not all optical elements in the lens use the nanostructure coatings and also the coatings themselves are not perfect. In spite of this, overall performance is quite impressive: the highest surface brightness ghost in the image (to the immediate right of Venus) contains only $\sim 0.025\%$ of the light from the planet. Our strategy for dealing with these features is to take advantage of the fact that their position depends on the optical path through the lenses, so we can offset individual cameras slightly and average the features out when images are combined. This takes advantage of the redundancy at the heart of the array design, and this aspect of the instrument concept also plays a key role in mitigating the effects of imperfect flat fielding and time-dependent additive atmospheric contributions to the images. In practice, summed images are flat to better than 0.1% of the sky level. Readers interested in the methodology for the data reduction procedure currently used with the Dragonfly Telephoto Array data are referred to van Dokkum, Abraham & Merritt (2013).

5. Sensitivity

The rate of detected photons per pixel, Φ, from an object with surface brightness $S_\lambda(\lambda)$ is given by:

$$\Phi = a \left(\frac{D}{L}\right)^2 \int \frac{E(\lambda) S_\lambda(\lambda)}{h\nu} e^{-k(\lambda)\sec Z} d\lambda \quad (3)$$

where a is the area of a pixel, D is the effective aperture, L is the system focal length, $E(\lambda)$ is the total system efficiency, $\sec Z$ is the air mass and $k(\lambda)$ is the extinction coefficient of the atmosphere. We can convert this equation into a more immediately useful form by: (i) ignoring extinction; (ii) noting that (D/L) is the inverse of the focal ratio f; (iii) replacing the functions inside the integral by their mean values within the filter bandpass $\Delta\lambda$; and (iv) converting the frequency in the denominator to an equivalent wavelength. This gives:

$$\Phi \approx a\ f^{-2}\ \frac{\bar{E}\bar{S}_\lambda}{hc} \bar{\lambda}\ \Delta\lambda \quad (4)$$

which reinforces the point noted earlier that the detected photon rate per pixel varies inversely with the square of the focal ratio. This is of course the central reason why the Dragonfly Telephoto Array (effectively an $f/1$ system in its current configuration) is quite efficient[16].

The surface brightness in equation 4 can be cast into units of mag/arcsec^2 by noting that $\bar{S}_\lambda = \bar{F}_0 \times 10^{-0.4\mu}$, where $\bar{F}_0$ is the flux zero point for the filter and μ is the mean surface brightness in magnitude units in the bandpass. In the AB system the zeroth magnitude calibrator is defined in frequency space as 3631 Jy in all bands, so after conversion back to wavelength space $\bar{F}_0 = (3631\ \mathrm{Jy/arcsec^2}) \times c/\bar{\lambda}^2$ where $\bar{\lambda}$ is the effective wavelength of the filter. Substituting this into equation 4 and rearranging, we obtain:

$$\Phi \approx \frac{a\ f^{-2}\ \bar{E}\ (3631\ \mathrm{Jy/arcsec^2})\ 10^{-0.4\mu}}{h} \left(\frac{\Delta\lambda}{\bar{\lambda}}\right) \quad (5)$$

Before inserting numerical values into this equation it is important to note two things:

1. The transmission curve of an interference filter is a function of the beam speed. Because the beam of the telephoto lenses used in the Dragonfly Array is quite fast, some care needs to be taken before using manufacturer's scans obtained using a collimated beam to define $\bar{\lambda}$ and $\Delta\lambda$. The change in the transmission curve as a function of beam speed is a function of the specific recipe used to construct the dielectric layer stack in the filter. However, in general, as the beam speed increases the transmission curve shifts very slightly blueward and the peak throughput drops.[17] The latter effect is seen

[16] Of course equation 4 also shows that a slow optical system can increase its detected photon rate by detector binning. For survey instruments there is generally an étendue conservation trade to be made between aperture, focal ratio and desired spatial resolution.

[17] An approximate expression for the shift in central wavelength is $\bar{\lambda}_{\mathrm{eff}} = \bar{\lambda}(1 - \frac{\beta^2}{4n^2})$ where $\bar{\lambda}_{\mathrm{eff}}$ is the shifted central wavelength, n is the average index of refraction for the mul-

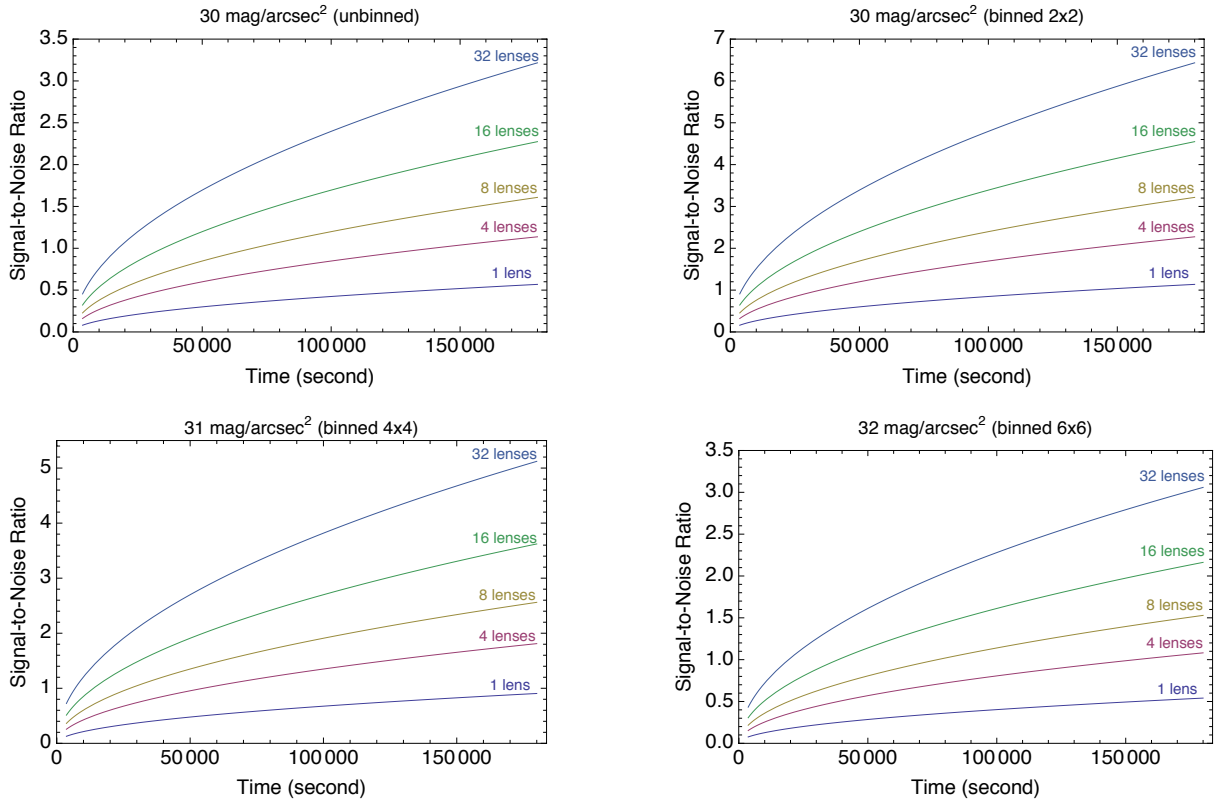

Fig. 9.— SDSS g-band signal-to-noise ratio as a function of integration time for various configurations of the Dragonfly Telephoto Array. Individual panels correspond to targets with surface brightness and binning factors of (top-left:) 30 mag/arcsec^2 with no binning; (top-right:) 30 mag/arcsec^2 binned 2x2; (bottom-left:) 31 mag/arcsec^2 binned 4x4; (bottom-right:) 32 mag/arcsec^2 binned 6x6. different surface brightness and binning factor. The lines on individual panels correspond to the performance of 32-lens, 16-lens, 8-lens (current configuration), 4-lens, and 1-lens systems. All panels assume a g-band sky surface brightness of 22.5 mag/arcsec^2, which is the darkest sky expected at the New Mexico Skies telescope hosting facility at solar minimum.

fairly clearly in Figure 2 when comparing the Astrodon filter measurements made with a collimated beam to CFHT MegaCam measurements made with an $f/8$ beam. We do not (yet) have transmission curves measured at $f/2.8$, but the CFHT MegaCam filter transmission curves are likely to be a closer approximation to the actual transmission of the filters in our configuration than are the Astrodon curves. We therefore use the CFHT MegaCam throughput curves in our calculations of the throughput of the Canon lenses given below.

2. There is some ambiguity in the literature regarding the definitions of filter effective wavelengths and bandpasses. In the present context, we define the effective wavelength to be the mean wavelength:

$$\bar{\lambda} = \int \lambda \ \phi(\lambda) \ d\lambda \qquad (6)$$

where ϕ is the transmission curve normalized to unit area. We define the bandpass $\Delta\lambda$ to mean the full-width at half maximum obtained by approximating the normalized transmission curve by a gaussian, which gives:

$$(\Delta\lambda)^2 = 8 \ln 2 \int (\lambda - \bar{\lambda})^2 \ \phi(\lambda) \ d\lambda. \qquad (7)$$

With these definitions, the SDSS g and r-band transmission curves based on CFHT MegaCam measurements shown in Figure 2 give $\bar{\lambda} = 485.7$nm and $\Delta\lambda = 100.2$nm (g-band) and $\bar{\lambda} = 627.3$nm and $\Delta\lambda = 84.2$nm (r-band).

Inserting numerical values into equation (5) we obtain the following count rates, corresponding to $\mu = 0$ mag/arcsec^2 at the top of the atmosphere in g and r-band, respectively:

$$\Phi_g = 1.79 \times 10^9 \ N \ \bar{E} \text{ photon/pix/s} \qquad (8)$$

$$\Phi_r = 1.16 \times 10^9 \ N \ \bar{E} \text{ photon/pix/s.} \qquad (9)$$

In these expressions N is the number of lenses in the array, and $\bar{E}$ is the mean efficiency. These equations can be used to compute the efficiency of the lenses from measured instrumental zero points and appropriate corrections for extinction.

Comparing the count rates in equations (8) and (9) with observations made on August 1, 2013, we find that the overall efficiency of the Dragonfly Array was 34% in g-band and 35% in r-band, with individual lenses varying by 1–2 percent around these values[18]. These observations were made several months after cleaning, and in our experience freshly cleaned lenses improve upon these numbers by several percent. These observed efficiencies should be compared with the maximum efficiency achievable (43% in both g and r-bands) based on the throughput curves for the filters and the quantum efficiency of the detector shown in Figure 2. We conclude that a lower limit for the overall transmittance of freshly cleaned[19] lenses is 85%, and the weak link in the overall efficiency of the system at present is the relatively low quantum efficiency of the commercial CCD cameras used. Improving these is an obvious upgrade for the array.

Unlike most imaging systems, the Dragonfly Telephoto Array is designed to grow in effective aperture with time as additional lenses are added to the system. An attempt to translate the performance of the Dragonfly Telephoto Array into

tiple layers of dielectric in the stack, and β is the the cone angle (the maximum incidence angle of light in the filter). The cone angle is related to focal ratio by $\sin\beta \sim 1/(2f)$. The loss in peak transmission is more difficult to model and we are unaware of any simple 'rule of thumb' approximation for this.

[18] We incorporated 0.39 mag of g-band extinction and 0.21 mag of r-band extinction into the estimates. These values were calculated by summing Rayleigh scattering, ozone absorption and aerosol pollutant terms. We note that the aerosol (microscopic particulate) term is often neglected, but it is often important; for example, in summer it is often the dominant term for observatories located in the Southwestern USA because of forest fires. It is straightforward to determine the needed correction for particulates from aerosol optical depth maps produced by the Moderate Resolution Imaging Spectroradiometer (MODIS) on the NASA Terra/EOS-AM satellite. At the present time, nightly MODIS maps are available here: http://www.star.nesdis.noaa.gov/smcd/spb/aq/index.php.

[19] An interesting advantage of an all-refractive design is that it is less sensitive to dirt. A dirty objective decreases throughput without much of an an impact on contrast because the dominant scattering mode is backwards and out of the optical path. On the other hand, scattering from a reflective objective is more pernicious, because it scatters light back into the beam. In other words, dust on reflective surfaces not only dims the view, it also reduces contrast by increasing the sky background.

signal-to-noise ratio as a function of source surface brightness, integration time, array size, and binning factor is shown in Figure 9. This figure makes two important points. The first of these is that, because the system is not limited by systematic errors, integration times in excess of 100ks are entirely realistic. The second is that even with the array in its present configuration, surface brightness levels well below 30 mag/arcsec^2 are easily achievable. By trading off resolution, surface brightnesses below 32 mag/arcsec^2 are realistically achievable by binning images with the current array. Alternatively, one could simply upgrade the array to incorporate more lenses. In any case, undertaking a survey of around 100 galaxies to the surface brightness limits needed to test the predictions of galaxy formation models is feasible, but will require the present array to be operated in a survey mode for several years. We have embarked on such a survey, and the first results from this campaign are presented in van Dokkum, Abraham & Merritt 2013 (submitted).

6. Summary

The Dragonfly Telephoto Array is an innovative instrument concept whose goal is to open up a new observational regime: ultra low surface brightness imaging at visible wavelengths. The array is comprised of multiple commercial 400mm $f/2.8$ telephoto lenses which have high performance subwavelength nano-fabricated optical coatings designed to minimize scattered light and ghosting. The array is presently comprised of eight lenses, though we anticipate adding additional lenses in the future. In this paper we have outlined the basic concept and reported on the performance of the 8-lens array, which is similar to that of a 0.4 m aperture $f/1.0$ refractor with a $2.6^\circ \times 1.9^\circ$ field of view. The imager has scattering and ghosting properties an order of magnitude better than those of the best reflectors optimized for low surface brightness imaging. Harnessing this new capability, the Dragonfly Telephoto Array is now executing a fully-automated multi-year imaging survey of a sample of nearby galaxies in order to undertake the first census of ultra-faint substructures in galaxies in the nearby Universe. The detection of structures at these surface brightness levels may hold the key to solving the 'missing substructure' and 'missing satellite' problems of conventional hierarchical galaxy formation models.

Acknowledgments
We are indebted to the Dunlap Institute of the University of Toronto, Yale University, and NSERC for financial support of this project. We particularly thank Peter Martin and James Graham, the acting and former directors of the Dunlap Institute at the University of Toronto, for their moral and financial support and excellent technical advice. PhD students Jielai Zhang (Toronto) and Allison Merritt (Yale) deserve many thanks for engineering work, for debugging, and for late nights observing. Dana Simard (Queens University) is thanked for her work in developing the Dragonfly Web App.

René Doyon and Robert Lamontagne of the Université de Montréal deserve our thanks for allowing us to undertake the initial testing of the lenses used in this project at the Observatoire du Mont Mégantic.

We are grateful for all the help provided by the staff at New Mexico Skies, and for their outstanding professionalism in support of this project. We particularly thank Mike Rice and Lynn Rice, owners of facility, and site engineers Randy Reimers and Grady Owens, for superb support and for innumerable late night fixes to the Dragonfly Telephoto Array. Thanks are also due to Erik Widding of Birger Engineering and Don Goldman of Astrodon Imaging for supplying us with customized focus controllers and filters for this project. We are also grateful to Software Bisque for supplying us with an excellent Paramount ME II mount on short order, and to Matthew Bisque for technical assistance.

This project emerged as a result of a bet[20] made by RGA and PGvD at the Mount Everest Nepalese Restaurant on Bloor Street in Toronto. We thank the United Breweries Group of Bangalore for providing us with inspiration on the night in question.

[20] RGA lost.

Appendix 1 – Example of a nightly control script

```
#!/bin/sh

# Edit this script in the afternoon, set it running, then get your data tomorrow.
#
# To observe a target specified by name, use the 'auto_observe' command below. This pretty
# much does everything for you. To be more specific: 'auto_observe' monitors the state of the
# observatory and only integrates if the weather is good enough for the
# roof to be open. If the weather is not good enough it simply sleeps for for the equivalent
# exposure time and then continues at the next step in the sequence, checking the weather
# as it goes along. Once observing commences, the script focuses all of the
# cameras then executes a 9-point dither pattern with 600s integrations. Guide stars
# are acquired as needed. A dark frame is obtained at the end of the sequence.
# Focus is adjusted as needed. At the end of the sequence all-sky camera
# images, image quality estimates, and other log information is emailed to the
# Dragonfly account.

######### Startup settings - do not edit the next set of lines #########

source "/usr/local/bin/df_library.sh"   # Load library
all_set_path                            # Automatically set data location
df_sleep_until_twilight                 # Pause until twilight
df_startup                              # Activate system with best-guess focus positions
all_regulate -10                        # Set CCD temperature
auto_flats                              # Automatic flats with 5000-15000 ADU in r'-band

######### EDIT BELOW HERE #########

sleep_until 0256                        # Set to end of nautical twilight in UTC

# Observe M101 tonight. The moon rises in about 6h so stop then.

auto_observe "M 101"                    # This line takes about 2h to execute
auto_observe "M 101"
auto_observe "M 101"

######### DO NOT EDIT BELOW HERE #########

# Done observing. Shut down gracefully.
if [ -e "INTERRUPT.txt" ]
then
  exit
else
  mount park
  power 12V off
fi
```

REFERENCES

Atkinson, A. M., Abraham, R. G., & Ferguson, A. M. N. 2013, ApJ, 765, 28

Barton, I. J. & Thompson, L. A. 1997, AJ, 114, 655

Belokurov, V., Evans, N. W., Irwin, M. J., Lynden-Bell, D., Yanny, B., Vidrih, S., Gilmore, G., Seabroke, G., Zucker, D. B., Wilkinson, M. I., Hewett, P. C., Bramich, D. M., Fellhauer, M., Newberg, H. J., Wyse, R. F. G., Beers, T. C., Bell, E. F., Barentine, J. C., Brinkmann, J., Cole, N., Pan, K., & York, D. G. 2007, ApJ, 658, 337

Bertin, E. & Arnouts, S. 1996, A&AS, 117, 393

Cooper, A. P., Cole, S., Frenk, C. S., White, S. D. M., Helly, J., Benson, A. J., De Lucia, G., Helmi, A., Jenkins, A., Navarro, J. F., Springel, V., & Wang, J. 2010, MNRAS, 406, 744

Cooper, A. P., D'Souza, R., Kauffmann, G., Wang, J., Boylan-Kolchin, M., Guo, Q., Frenk, C. S., & White, S. D. M. 2013, ArXiv e-prints

Dubinski, J., Mihos, J. C., & Hernquist, L. 1996, ApJ, 462, 576

Fry, A. M., Morrison, H. L., Harding, P., & Boroson, T. A. 1999, AJ, 118, 1209

Ibata, R., Irwin, M., Lewis, G., Ferguson, A. M. N., & Tanvir, N. 2001, Nature, 412, 49

Johnston, K. V., Bullock, J. S., Sharma, S., Font, A., Robertson, B. E., & Leitner, S. N. 2008, ApJ, 689, 936

Kazantzidis, S., Bullock, J. S., Zentner, A. R., Kravtsov, A. V., & Moustakas, L. A. 2008, ApJ, 688, 254

Kormendy, J. & Bahcall, J. N. 1974, AJ, 79, 671

Martínez-Delgado, D., Gabany, R. J., Crawford, K., Zibetti, S., Majewski, S. R., Rix, H.-W., Fliri, J., Carballo-Bello, J. A., Bardalez-Gagliuffi, D. C., Peñarrubia, J., Chonis, T. S., Madore, B., Trujillo, I., Schirmer, M., & McDavid, D. A. 2010, AJ, 140, 962

McConnachie, A. W., Irwin, M. J., Ibata, R. A., Dubinski, J., Widrow, L. M., Martin, N. F., Côté, P., Dotter, A. L., Navarro, J. F., Ferguson, A. M. N., Puzia, T. H., Lewis, G. F., Babul, A., Barmby, P., Bienaymé, O., Chapman, S. C., Cockcroft, R., Collins, M. L. M., Fardal, M. A., Harris, W. E., Huxor, A., Mackey, A. D., Peñarrubia, J., Rich, R. M., Richer, H. B., Siebert, A., Tanvir, N., Valls-Gabaud, D., & Venn, K. A. 2009, Nature, 461, 66

Mihos, J. C., Harding, P., Feldmeier, J., & Morrison, H. 2005, ApJ, 631, L41

Mihos, J. C., Harding, P., Spengler, C. E., Rudick, C. S., & Feldmeier, J. J. 2013, ApJ, 762, 82

Moore, B., Lake, G., Quinn, T., & Stadel, J. 1999, MNRAS, 304, 465

Naab, T., Johansson, P. H., Ostriker, J. P., & Efstathiou, G. 2007, ApJ, 658, 710

Nelson, P. G., Tomczyk, S., Elmore, D. F., & Kolinski, D. J. 2008, in Society of Photo-Optical Instrumentation Engineers (SPIE) Conference Series, Vol. 7012, Society of Photo-Optical Instrumentation Engineers (SPIE) Conference Series

Roddier, C. & Roddier, F. 1993, Journal of the Optical Society of America A, 10, 2277

Slater, C. T., Harding, P., & Mihos, J. C. 2009, PASP, 121, 1267

Tal, T., van Dokkum, P. G., Nelan, J., & Bezanson, R. 2009, AJ, 138, 1417

Toomre, A. & Toomre, J. 1972, ApJ, 178, 623

van Dokkum, P. G. 2005, AJ, 130, 2647

Wallace, P. T. 1994, in Astronomical Society of the Pacific Conference Series, Vol. 61, Astronomical Data Analysis Software and Systems III, ed. D. R. Crabtree, R. J. Hanisch, & J. Barnes, 481

This 2-column preprint was prepared with the AAS LaTeX macros v5.0.